

Robust Active Visual Perching with Quadrotors on Inclined Surfaces

Jeffrey Mao¹, Stephen Nogar², Christopher Kroninger², and Giuseppe Loianno¹

Abstract—Autonomous Micro Aerial Vehicles are deployed for a variety of tasks including surveillance and monitoring. Perching and staring allow the vehicle to monitor targets without flying, saving battery power and increasing the overall mission time without the need to frequently replace batteries. This paper addresses the Active Visual Perching (AVP) control problem to autonomously perch on inclined surfaces up to 90° . Our approach generates dynamically feasible trajectories to navigate and perch on a desired target location, while taking into account actuator and Field of View (FoV) constraints. By replanning in mid-flight, we take advantage of more accurate target localization increasing the perching maneuver's robustness to target localization or control errors. We leverage the Karush-Kuhn-Tucker (KKT) conditions to identify the compatibility between planning objectives and the visual sensing constraint during the planned maneuver. Furthermore, we experimentally identify the corresponding boundary conditions that maximize the spatio-temporal target visibility during the perching maneuver. The proposed approach works on-board in real-time with significant computational constraints relying exclusively on cameras and an Inertial Measurement Unit (IMU). Experimental results validate the proposed approach and show the higher success rate as well as increased target interception precision and accuracy with respect to a one-shot planning approach, while still retaining aggressive capabilities with flight envelopes that include large excursions from the hover position on inclined surfaces up to 90° , angular speeds up to 750 deg/s , and accelerations up to 10 m/s^2 .

Index Terms—Aerial Robotics, Perception-Aware Planning, Vision for robotics

I. INTRODUCTION

MICRO Aerial Vehicles (MAVs) such as quadrotors have great speed and maneuverability while being able to hover in place. This makes them ideal for monitoring and surveillance. However, they tend to have very low flight time in the 20 – 30 minutes range. By perching on a surface, a quadrotor can extend its mission time and save power while still monitoring one or multiple targets. This motivates the need for autonomous perching solutions. Inclined flat surfaces like walls and rooftops are plentiful especially in urban environments and by focusing on this avenue, we aim to greatly reduce the energy consumption for multiple types of missions. Several challenges complicate the perching maneuver execution. The quadrotor is an underactuated system where both orientation and acceleration of the vehicle are dependent

on each other. In addition, during the maneuver the vehicle requires large excursions from the hover position. In our previous work [1], we started to address these two challenges. Our solution was capable of perching on planar surfaces up to 90° solely using on-board sensing and computation as shown in Fig. 1. However, it presented three main drawbacks. First, target localization is strongly affected by bad or partial target visibility as well as by target distance. Second, perching on 90° inclined surfaces requires aggressive motions from the hovering position which in turn may cause higher estimation and control error. This aspect is further complicated by the fact that our platform only uses on-board cameras with limited resolution and a low cost IMU to localize the vehicle and the target. Third, our solution does not enforce the target visibility during the planned maneuver which can be exploited to refine the trajectory during the perching maneuver in an active fashion. This work, compared to our previous conference paper [1], addresses the aforementioned challenges by proposing a mid-flight Active Visual Planning (AVP) approach. Our original work [1] would detect the target and then plan a perching trajectory based on a target localization without taking advantage of additional target measurements that can be obtained during the maneuver to improve perching precision and accuracy. AVP involves planning a new perching trajectories based on the quadrotors subsequent target localization during flight in real-time. In the presented case, the replanning procedure is performed on-board at 30 Hz until the target is intercepted. Our algorithm provides three key benefits. First, it solves the perception error by exploiting better target localization as the robot-target distance reduces. Second, it reduces the burden on our controller to close control error by replanning the whole trajectory from the current offset course to the target enabling accurate landing. Third, the sum of our replanned trajectories naturally favors trajectories with reduced spatial distance compared to a one-shot planning approach which further facilitates target's interception.

This paper presents multiple contributions. First, we present a framework for agile autonomous quadrotor perching on planar surfaces up to 90° inclinations. This approach is highly robust to sensor and control noises compared to a one-shot planning approach presented in our previous work [1]. Second, the proposed approach allows the quadrotor to plan trajectories in mid-flight for perching based on consecutive target localization information providing robustness to target localization errors. Third, our strategy enforces the target visibility within the camera Field of View (FoV) to ensure the landing pad remains in sight. We exploit Karush-Kuhn-Tucker (KKT) conditions to verify the compatibility between the FoV

¹The authors are with the New York University, Tandon School of Engineering, Brooklyn, NY 11201, USA email: {jm7752, loiannog}@nyu.edu.

²The authors are with the DEVCOM Army Research Laboratory, 2800 Powder Mill Road, Adelphi, MD 20783, USA. email: {stephen.m.nogar, christopher.m.kroninger}.civ@army.mil.



Figure 1. Aggressive visual perching sequence maneuver for a 90° inclined surface [1].

constraint, the perching maneuver objectives, and additional actuator and sensing constraints to ensure the planned trajectory is both dynamically and physically feasible. Furthermore, we experimentally identify the boundary conditions that can maximize the spatio-temporal target visibility during the maneuver. Finally, our solution is lightweight and run solely on-board limited computational unit without any external sensors or computation at 30 Hz. Multiple experimental results demonstrate that the proposed approach is able to achieve more consistent and accurate target interception for planar targets up to 90° inclinations compared to one-shot planning approach [1].

II. RELATED WORKS

Perching on a vertical surface is a challenging problem because quadrotors are nonholonomic and underactuated systems where orientation depends on the linear acceleration. As a result, the perching maneuver on steep inclined surfaces like 90° requires high angular momentum which induces target loss and camera motion blur making the localization, control, and planning problem extremely challenging. This has led to two main research avenues. The first one focuses on the planning and control problems to generate feasible aggressive maneuvers. Many of these works use external sensors to localize the quadrotor and target during aggressive maneuvers. The second addresses the mechanical platform design proposing novel mechanisms or attachments to ease perching on specific structures. This simplifies the perching problem, but increases the vehicle's mass by 10% – 40%.

Related to planning, [2] details how to using polynomial splines to formulate a trajectory on the flat outputs $\{x, y, z, \psi\}$ or position in the inertial frame and yaw. Further optimizations using different polynomial splines and additional costs have been proposed for solving time optimal trajectories by [3, 4, 5]. However, these works purely focus on the planning problem for aerial navigation without studying the appropriate planning constraints to resolve the perching problem. More complex planners [6, 7] propose approaches on SE(3) which generate feasible trajectories on both rotation and translation. However, these works require substantially more computation than planning on the flat outputs and are unsuitable for on-board computation on small-scale robots with limited computational units that we employ in this work. Furthermore, works as [8, 9, 10] plan trajectories on the full robot state, but are even more computationally expensive than [6, 7] taking on the order of minutes to solve a single trajectory. Our current work is most similar to [11, 12, 1] parameterizing the trajectory on the flat outputs and formulating the perching constraint

as an acceleration constraint. However, we also apply active vision feedback in our planner to refine our trajectory which to the best of our knowledge has not been proposed to solve a perching problems with up to 90° inclined surfaces. There are also specialized controllers that perform similar aggressive maneuvers such as multiple flips in [13, 14]. These controllers tend to be fairly narrow and designed to solely execute one maneuver such as multiple flips. They tend to not generalize very well if a different maneuver is required such as perching at a different incline and require motion capture systems. Conversely, [15] the authors performed aggressive motions such as quadrotor flips using purely on-board sensor, but this is based on a deep learning approach which is still very computationally expensive to run on-board small-scale robots and does not present guarantees. Other works focus on a much simpler target interception while relying purely on on-board camera. Visual Servoing approaches [16, 17] have shown controllers capable of landing on targets through purely visual feedback, but these methods are highly dependent on objects' shapes and require the object to continuously be in the FoV to preserve the control stability. Therefore, most of the maneuver are not aggressive and do not present large excursions from the hover position as in the proposed case.

Related to mechanical design, there are also a variety of perching mechanism designs to simplify high incline landing such as claws [18, 19, 20] for cylindrical objects, dry adhesives [21, 22, 23], suction gripper mechanisms [24], arms attached to the quadrotor [25, 26], electroadhesive material [27], or other passive mechanisms [28]. However adding additional mechanisms further increase the vehicle's mass, inertia, and energy requirements while concurrently decreasing the overall flight time. This mass increase can range from 10% in [25] to 40% in [28].

Finally, fixed wing solutions for vertical perching have also been proposed [29, 30, 31]. Fixed wing aircrafts tend to be much less maneuverable than quadrotor being unable to hover in place and much bulkier in comparison. The flight time is more restricted with respect to fixed wing solutions further motivating the usefulness to provide autonomous perching solutions for quadrotors.

Our previous work [1] considered the on-board state estimation, planning, target localization, and control problem for aggressive perching generating dynamically and physically feasible trajectories. However, the target localization relied only on a single image detection. Therefore, the localization was strongly affected by the robot-target relative distance and degraded at further distances due to relying on one Apriltag localization [32]. Our current work ensures dynamic and physical feasibility in the planned path, does not require external sensors, and performs repeated Apriltag localization [32] and planning to refine in an active fashion the robot's motion during the maneuver to increase the perching accuracy at longer distances and robustness to both control and localization errors. Several works [33, 34] consider the mid flight replanning problem, but they are specifically designed for navigation and obstacle avoidance. Finally, [35] does involve using vision to plan new trajectories to intercept a moving target, but the problem is specifically designed for the simple

landing 0° (horizontal) inclined surfaces case.

III. SYSTEM OVERVIEW

The proposed system architecture is shown in Fig. 3. The platform is a quadrotor running with a Qualcomm[®] Snapdragon[™] board and 4 brushless motors. The Qualcomm[®] Snapdragon[™] consists of a Qualcomm[®] Hexagon[™] DSP, Wi-Fi, Bluetooth, GPS, four core processor, IMU, and two cameras: a downward facing 160° FoV and a front-facing 70° FOV. For perching, we employ VELCRO[®] material mounted in the ventral part of the vehicle. This includes an improved landing gear design to increase the support for the VELCRO[®] attachment.

The software framework is developed in ROS¹ Indigo on a Linux kernel. Our frame includes a state estimation algorithm running at 300 Hz composed of a Unscented Kalman Filter (UKF) and Visual Inertial Odometry (VIO) [12], which processes images from the downward facing camera at 30 Hz. The downward facing camera is solely devoted to state estimation of the quadrotor, whereas the front-facing camera is used to localize the target at a rate of 10 Hz. Furthermore, the system runs on-board a position and attitude controllers as well as a trajectory planner along with the target localization and state estimation.

As shown in Fig. 2, we define the inertial frame \mathcal{I} , by the three axes $[\mathbf{e}_1 \ \mathbf{e}_2 \ \mathbf{e}_3]$. The quadrotor body frame, \mathcal{B} , is defined by $[\mathbf{b}_1 \ \mathbf{b}_2 \ \mathbf{b}_3]$. The target frame, \mathcal{S} , is represented by the axes $[\mathbf{s}_1 \ \mathbf{s}_2 \ \mathbf{s}_3]$. Similarly, we define the position of the quadrotor's center of mass in the inertial frame as $\mathbf{x} = [x \ y \ z]^\top$, and the target's center as $\mathbf{s} = [s_x \ s_y \ s_z]^\top$. The perching problem requires the vehicles to plan and execute a feasible trajectory (i.e., generating a sequence of $\mathbf{R}(t) \in SO(3)$ and $\mathbf{x}(t) \in \mathbb{R}^3$) in a predefined time frame, $t \in [t_0, t_f]$, such that both $\mathcal{B} \equiv \mathcal{S}$ and $\mathbf{x} = \mathbf{s}$ are reached at $t = t_f$. This is achieved in a loop structure demonstrated in Fig. 3. First, the vehicle visually locates the target and estimates the relative configurations from the \mathcal{B} to \mathcal{S} frames (i.e., relative position $\mathbf{p}_S^B \in \mathbb{R}^3$ and orientation $\mathbf{R}_S^B \in SO(3)$). Second, the relative configuration information is incorporated at the planning and control levels to generate and execute trajectories that are dynamically and physically feasible. Finally, the system loops back to the initial step with an updated target and quadrotor localization. This loop continues until the quadrotor has intercepted the target.

IV. CONTROL, ESTIMATION, AND PLANNING

The quadrotor's system dynamic model in the inertial frame \mathcal{I} is

$$\begin{aligned} \dot{\mathbf{x}} &= \mathbf{v}, \dot{\mathbf{v}} = \mathbf{a}, m\mathbf{a} = \mathbf{R}\tau\mathbf{e}_3 - m\mathbf{g}\mathbf{e}_3, \\ \dot{\mathbf{R}} &= \mathbf{R}\hat{\boldsymbol{\Omega}}, \mathbf{J}\dot{\boldsymbol{\Omega}} + \boldsymbol{\Omega} \times \mathbf{J}\boldsymbol{\Omega} = \mathbf{M}, \end{aligned} \quad (1)$$

where $\mathbf{x}, \mathbf{v}, \mathbf{a} \in \mathbb{R}^3$ are the position, velocity, acceleration of the quadrotor's center of mass in Cartesian coordinates with respect to the inertial frame \mathcal{I} , \mathbf{R} represents the orientation of the quadrotor with respect to \mathcal{I} . $\boldsymbol{\Omega} \in \mathbb{R}^3$ is the angular

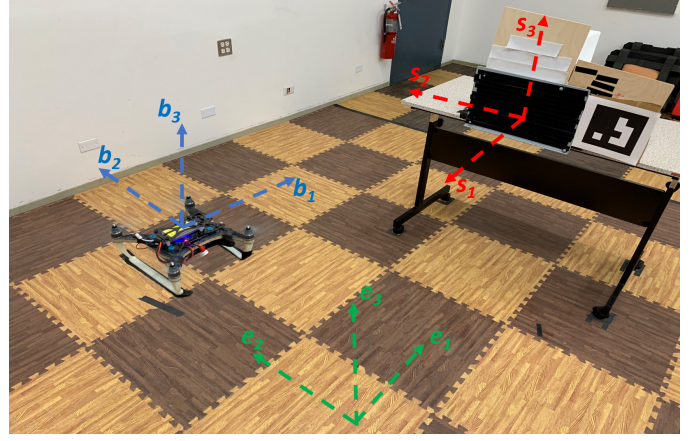


Figure 2. Visualization of the quadrotor, inertial, and target frame.

velocity of the quadrotor with respect to \mathcal{B} , $m \in \mathbb{R}$ denotes the mass of the quadrotor, $\mathbf{J} \in \mathbb{R}^{3 \times 3}$ represents its inertial matrix with respect to \mathcal{B} , $g = 9.81m/s^2$ is the standard gravitational acceleration, $\mathbf{M} \in \mathbb{R}^3$ is the total moment with respect to \mathcal{B} , $\tau \in \mathbb{R}$ represents the total thrust to the quadrotor, and the $\hat{\cdot}$ represents the mapping such that $\hat{\mathbf{a}}\mathbf{b} = \mathbf{a} \times \mathbf{b}, \forall \mathbf{a}, \mathbf{b} \in \mathbb{R}^3$.

To achieve aggressive maneuvers, we apply a nonlinear geometric controller that was leveraged from our previous work [36] to achieve agile flight in an indoor environments. Thrust τ and moment \mathbf{M} are the control inputs selected as

$$\begin{aligned} \tau &= (-\mathbf{k}_x\mathbf{e}_x - \mathbf{k}_v\mathbf{e}_v + m\mathbf{g}\mathbf{e}_3 + m\ddot{\mathbf{x}}) \cdot \mathbf{R}\mathbf{e}_3 = \mathbf{f} \cdot \mathbf{R}\mathbf{e}_3, \\ \mathbf{M} &= -\mathbf{k}_R\mathbf{e}_R - \mathbf{k}_\Omega\mathbf{e}_\Omega + \boldsymbol{\Omega} \times \mathbf{J}\boldsymbol{\Omega} \\ &\quad - \mathbf{J} \left(\hat{\boldsymbol{\Omega}}\mathbf{R}^\top \mathbf{R}_C \boldsymbol{\Omega}_C - \mathbf{R}^\top \mathbf{R}_C \dot{\boldsymbol{\Omega}}_C \right), \end{aligned} \quad (2)$$

where $\mathbf{k}_R, \mathbf{k}_\Omega, \mathbf{k}_x, \mathbf{k}_v \in \mathbb{R}^{3 \times 3}$ represent the feedback gains for the errors in orientation, angular velocity, position and velocity respectively as positive definite diagonal matrices. $\mathbf{e}_R, \mathbf{e}_\Omega, \mathbf{e}_x, \mathbf{e}_v \in \mathbb{R}^3$ are the orientation, angular velocity, position and velocity errors this is detailed in works [37, 38], and the \cdot_C are the command or desired values obtained from the planning algorithm as shown in Section V-A1.

Vehicle localization is performed in the inertial frame \mathcal{I} through combining visual and inertial data via Visual Inertial Odometry (VIO) and Unscented Kalman Filter (UKF) leveraged from our previous work [12] on aggressive maneuvers. Localizing the target is done using Apriltag localization [32] on the 16h5 Tag family with the front camera to detect a single large tag with a known offset from the main pad. The larger tag decreases localization error and allows us to leverage all of the landing pad's area for perching. For individual single trajectory planning, we leverage our previous work [1] to model the trajectory on the set of vehicle's flat output space, $\{\mathbf{x}, \psi\} = \{x, y, z, \psi\}$ where ψ is the yaw angle of the quadrotor or the rotation around the \mathbf{b}_3 axis. Each flat output trajectory is independent and represented using a polynomial spline. We give an example of a single dimension's spline

¹www.ros.org

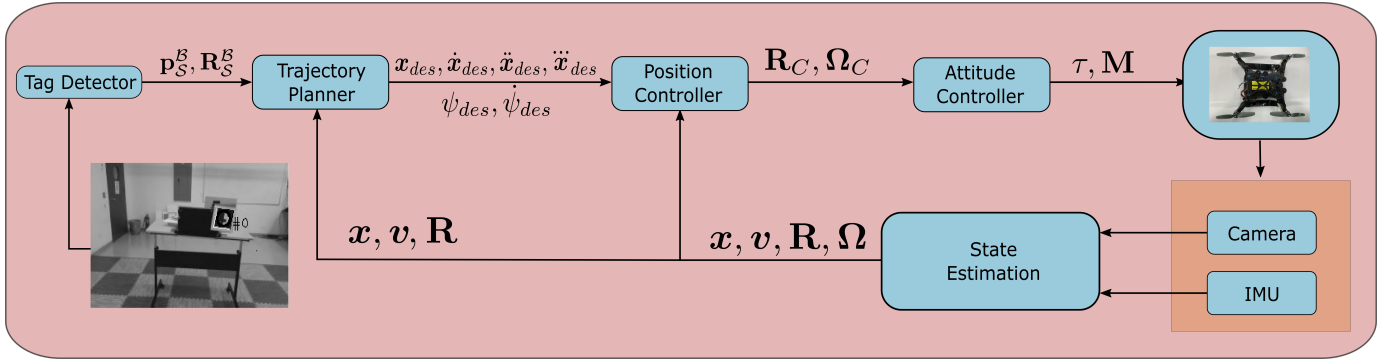


Figure 3. System architecture for the perching task.

defined as

$$P(t) = \begin{cases} p_1(t - t_0) & \text{if } t \in [t_0, t_1] \\ p_2(t - t_1) & \text{if } t \in [t_2, t_1] \\ \vdots & \\ p_f(t - t_{f-1}) & \text{if } t \in [t_{f-1}, t_f] \end{cases}, \quad (3)$$

$$p_i(t) = \sum_{n=0}^N c_{ni} t^n, \quad i = 1, \dots, f,$$

where p_i represents the i^{th} polynomial spline making up the full trajectory of P , $c_{ni} \in \mathbb{R}$ is the n^{th} coefficient of p_i , and N represents the polynomial order chosen for each spline. For our polynomial spline, we generate a reasonable guess at the required time needed for each spline. This formulation allows us to declare arbitrary constraints on the quadrotor's flat outputs and corresponding derivatives as linear constraints for any arbitrary time or time range as defined in [1]. We then minimize the squared norm of some derivative order defined as

$$\int_{t_0}^{t_f} \left\| \frac{d^j P(t)}{dt^j} \right\|^2 dt. \quad (4)$$

In our previous work [1], we show how to formalize this problem as a Quadratic Programming (QP) problem on the polynomial coefficients \mathbf{c} defined as

$$\begin{aligned} \min_{\mathbf{c}} \quad & \mathbf{c}^T \mathbf{Q} \mathbf{c}, \\ \text{s.t.} \quad & \mathbf{A} \mathbf{c} = \mathbf{b}, \\ & \mathbf{y} \leq \mathbf{G} \mathbf{c} \leq \mathbf{z}, \end{aligned} \quad (5)$$

where the matrices \mathbf{Q} is derived from the cost function in eq. (4), and the matrices \mathbf{A} , \mathbf{b} are derived from the equality constraint declared on flat outputs and corresponding derivatives for some arbitrary times, and \mathbf{y} , \mathbf{G} , \mathbf{z} on inequality constraints as defined in [1]. In the following section V-A, we describe the specific constraints for the Active Visual Perching problem. These constraints are the specific values needed to intercept the target as well as to maintain the target visibility in the camera FoV during the maneuver perching time.

V. ACTIVE VISUAL PLANNING

The goal of active visual planning is to be able to plan new trajectories mid-flight to increase robustness to sensor

and control disturbances and noises during aggressive flight by exploiting increased target localization accuracy and precision once the vehicle approaches the target. This strategy imposes two additional steps in the aforementioned planner. First, since the vehicle is planning while moving and the planning procedure takes a specific amount of time, we have to anticipate our flat output and corresponding time derivatives in the future when we swap the new trajectory. Second, we need to enforce the target visibility to guarantee and facilitate future replanning. This translates to a FoV constraint around the next replan time. The FoV constraint formulation and implementation is detailed in Section V-A1. In Fig. 4, we visualize the replanning procedure for one Cartesian axis, x . The same procedure is valid for the other axes. Our procedure can be broken into three steps: initial planning, anticipation of the next position, and replanning from the anticipated time and flat output along with corresponding derivatives. First, we have our initial trajectory formulated in step 1 with a set amount of time given to perching. Next in step 2, we detect our current position which is represented by the green star and t_{rp} , replan starting time represented by the red vertical line. Then, to take into account the overall replanning time duration on the vehicle's motion, we incorporate the quadrotor's flat output and corresponding derivatives with the spatio-temporal information by inferring the displacement of the quadrotor once the replanning ends as

$$\begin{aligned} \mathbf{x}_0 &= \mathbf{x}_n + P(t_{ex}) - P(t_{rp}), \\ \mathbf{v}_0 &= \mathbf{v}_n + \frac{dP(t_{ex})}{dt} - \frac{dP(t_{rp})}{dt}, \\ \mathbf{a}_0 &= \mathbf{a}_n + \frac{d^2P(t_{ex})}{dt^2} - \frac{d^2P(t_{rp})}{dt^2}. \end{aligned} \quad (6)$$

The quadrotor's position is represented by the purple star whereas the orange line represents the anticipated time of execution, t_{ex} . The anticipation, \mathbf{x}_0 , is done by calculating the spatial displacement that would occur in the original planned trajectory and adding it to the odometry position, \mathbf{x}_n . We repeat the same anticipation procedure for the velocity, \mathbf{v}_0 and acceleration \mathbf{a}_0 to get their respective values. Eq. (6) represents the procedure up to the second order derivative of the flat output for simplicity. This can be extended to any arbitrary order relevant in a specific problem. Finally in step 3, we plan a new trajectory from the flat outputs and corresponding derivatives with the new start time, t_{ex}

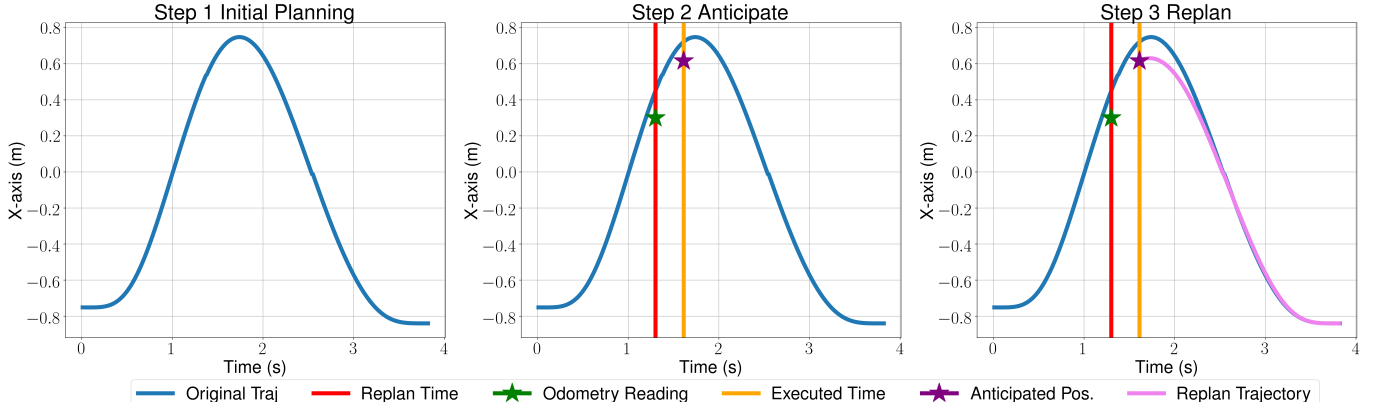


Figure 4. Repanning steps for one axis. This The horizontal axis is time, and the vertical is the X-axis distance. Blue represents the original trajectory. Red is when we start replanning. Orange is when we think the trajectory will take place. Green star is the current odometry. Purple star is the anticipated position. The pink trajectory is the new replanned trajectory.

including all relevant constraints detailed in Section (V-A) with the procedure mentioned in Section (IV). This process is repeated at a constant rate till target interception is achieved.

A. Active Visual Perching Constraints

In this section, we detail the specific planning constraints that are required to intercept the target at the end point and maintain line of sight to the target with our front camera. We also derive the additional constraints required to intercept the target and show how the choice of the target point's impact velocity influences the spatio-temporal target visibility during the maneuver. The above constraints represent inequality and equality constraints in the proposed optimization problem in eq. (5). Finally, we detail the procedure using the Sturm algorithm used to guarantee the actuator constraints are met.

1) *Field of View Constraint*: At a shorter distance, target localization improves as long as the target is in the FoV as quantified in Fig. 8. This motivates a FoV constraint to be imposed onto the quadrotor trajectory planning to maintain line of sight, so that the proposed AVP algorithm can exploit better localization. Our goal in this FoV constraint is to derive a linear constraint that is compatible with the optimization problem described in eq. (5) and ensures that the next time the quadrotor needs the target localization for planning it is in the correct position and orientation to view the target. Inspired by [39], we formulate our FoV constraint as a cone projected from the center of the drone's front camera. We can refer to Fig. 5 for a visualization. The relevant quantities for this constraint will be represented in the frame \mathcal{I} . First, \mathbf{x} and \mathbf{s} represent the drone and perching target's location. $\mathbf{n}_d = \mathbf{s} - \mathbf{x}$ represents the vector from the drone to the target. \mathbf{e}_c^Z represent the unit vector projected from the camera's center. \mathbf{n}_{proj} is the projection of \mathbf{n}_d on to \mathbf{e}_c^Z . Finally the ratio $\frac{r}{h}$ represents the ratio between the FoV cone's radius and height. To solve for \mathbf{n}_{proj} , we take the projection of \mathbf{n}_d on to \mathbf{e}_c^Z , such that \mathbf{e}_c^Z direction is maintained. This vector is $\mathbf{n}_{proj} = (\mathbf{n}_d^T \mathbf{e}_c^Z) \mathbf{e}_c^Z$. We can then define the FoV as a circle with a radius $\frac{r}{h} \|\mathbf{n}_{proj}\|_2$ and center at \mathbf{n}_{proj} . Finally, we wish to see if the target is inside the circular FoV, this finalizes our constraint as

$$\|\mathbf{n}_d - \mathbf{n}_{proj}\|_2 \leq \frac{r}{h} \|\mathbf{n}_{proj}\|_2. \quad (7)$$

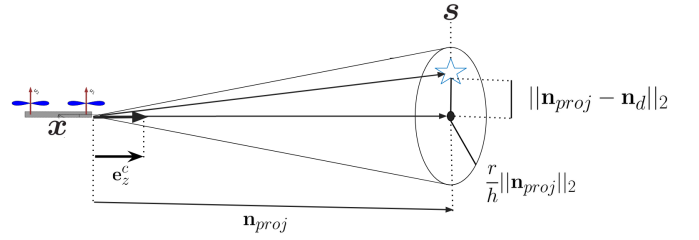


Figure 5. FoV constraint representation. \mathbf{x} is the quadrotor's position. \mathbf{s} and the star represents the target position

In order to apply this FoV constraint to our QP problem described in eq. (5), we use a Taylor Series expansion to linearize the inequality $\|\mathbf{n}_d - \mathbf{n}_{proj}\|_2 \leq \frac{r}{h} \|\mathbf{n}_{proj}\|_2$. Using the original nonlinear constraint would prevent us from arranging this as a QP optimization like in eq. (5). Using a nonlinear optimizer would take around 10 times the time required by the QP optimization. Given the optimization time on-board is 27 ms, a nonlinear optimization would take about 270 ms instead. This would mean we could only run our AVP algorithm at around 3Hz which is far slower than our target localization. The constraint is a function of the position, yaw, and acceleration. In other words, we can formulate $\|\mathbf{n}_d - \mathbf{n}_{proj}\|_2 \leq \frac{r}{h} \|\mathbf{n}_{proj}\|_2$ as $f(\mathbf{x}, \psi, \mathbf{a}) \leq g(\mathbf{x}, \psi, \mathbf{a})$. The Taylor series expansion of this constraint linearized around $(\mathbf{x}_0, \psi_0, \mathbf{a}_0)$ becomes

$$\begin{aligned} & (\nabla_f(\mathbf{x}_0, \psi_0, \mathbf{a}_0) - \nabla_g(\mathbf{x}_0, \psi_0, \mathbf{a}_0)) \begin{bmatrix} \mathbf{x} \\ \psi \\ \mathbf{a} \end{bmatrix} \leq \\ & g(\mathbf{x}_0, \psi_0, \mathbf{a}_0) - f(\mathbf{x}_0, \psi_0, \mathbf{a}_0) + \\ & (\nabla_f(\mathbf{x}_0, \psi_0, \mathbf{a}_0) - \nabla_g(\mathbf{x}_0, \psi_0, \mathbf{a}_0)) \begin{bmatrix} \mathbf{x}_0 \\ \psi_0 \\ \mathbf{a}_0 \end{bmatrix}, \end{aligned} \quad (8)$$

where ∇_f and ∇_g represent the gradients of $f(x)$ and $g(x)$ with respect to $[\mathbf{x}, \psi, \mathbf{a}]$. For our constraint, we select our linearization point, $(\mathbf{x}_0, \psi_0, \mathbf{a}_0)$, as the next values from the next point we replan from to ensure that the target is still in view. These values $(\mathbf{x}_0, \psi_0, \mathbf{a}_0)$ are calculated using

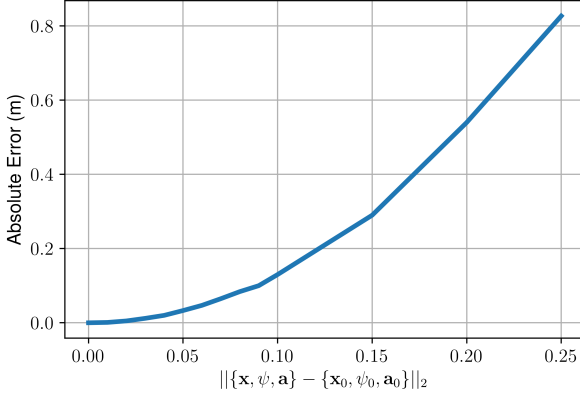


Figure 6. The linearization error of the field of view as a disturbance from the linearization zone.

eq. (6). Additionally, we impose an additional constraint on our position and acceleration during replanning such that

$$||\{\mathbf{x}, \psi, \mathbf{a}\} - \{\mathbf{x}_0, \psi_0, \mathbf{a}_0\}||_2 \leq 0.1, \quad (9)$$

as represented in Fig. 6. The combined constraint of eqs. (8) and (9) are added as inequality constraints in eq. (5). Fig. 6 details the Taylor series expansion error as a function of $||\{\mathbf{x}, \psi, \mathbf{a}\} - \{\mathbf{x}_0, \psi_0, \mathbf{a}_0\}||_2$. From this result, we notice that the Taylor series represents a good approximation of the original nonlinear constraint as long as this difference is below 0.1. Also another thing to note is that the proposed formulation of the linearized FoV constraint is independent from the replanning frequency. This is mainly due to the fact that we anticipate the next quadrotor's next flat output and corresponding derivatives when the next replan step will occur using eq. (6). Given a current time t when we plan, we know that the next time the AVP plan will be $t_* = t + dt$ where dt is the one divided by the AVP frequency. We can evaluate the original trajectory $p(t_*)$ and its derivatives to find position, acceleration, and yaw to act as a linearization position for our quadrotor with eq. (6). Because we linearize around t_* and not t , the FoV constraint is not directly dependent on the dt value.

Inspired by [12], we exploit the nonholonomic properties of the quadrotor and relate $\ddot{\mathbf{x}}$ and its orientation \mathbf{R} . From the transnational dynamics eq. (1), the thrust vector is a function of the quadrotor's acceleration.

$$\tau = m||\ddot{\mathbf{x}} + g\mathbf{e}_3||. \quad (10)$$

Because thrust can only be actuated on the plane normal the the propeller blades, the generated force is solely on \mathbf{b}_3 axis of the body frame of a quadrotor. From here we can derive that \mathbf{b}_3 should be

$$\mathbf{b}_3 = \frac{\ddot{\mathbf{x}} + g\mathbf{e}_3}{||\ddot{\mathbf{x}} + g\mathbf{e}_3||}. \quad (11)$$

To achieve successful perching, the quadrotor's body frame, \mathbf{B} , must align with the target's frame, \mathbf{R}_S , meaning $\mathbf{b}_3 = \mathbf{s}_3$ at the trajectory's end time, t_f . The \mathbf{s}_3 direction on the inclined surfaces is extracted from the last column of the matrix \mathbf{R}_S . This orientation \mathbf{R}_S is combining the target localization with

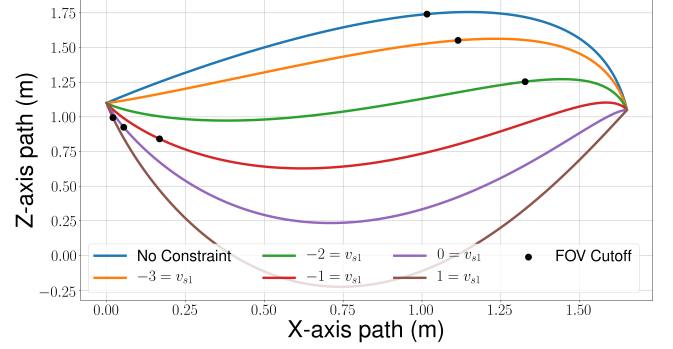


Figure 7. Visualization of each path for various \mathbf{v}_{S1} during 90° perching. $\mathbf{v}_{S1} = 1\text{m/s}$. The black dot is where the quadrotor loses sight of the target. Target's position is the end point of the trajectory. Velocities are in m/s.

respect to the body frame and the on-board localization of the body frame with respect to the inertial frame. Using eq. (11), we can declare this constraint as an acceleration as

$$\ddot{\mathbf{x}}(t_f) = \alpha\mathbf{s}_3 - g\mathbf{e}_3, \quad (12)$$

where $\alpha = ||\ddot{\mathbf{x}}(t_f) + g\mathbf{e}_3|| \in \mathbb{R}$ corresponds to the thrust's norm. The planned $\ddot{\mathbf{x}}$ is then set as a constraint for our optimization defined in eq. (5). To control the other two axis of the vehicle, $\mathbf{b}_1, \mathbf{b}_2$, we relate our desired \mathbf{R}_C to a desired yaw angle, ψ_{des} as

$$\begin{aligned} \mathbf{R}_C &= [\mathbf{b}_{1,C} \quad \mathbf{b}_{2,C} \quad \mathbf{b}_{3,C}] \\ \mathbf{b}_{1,C} &= \frac{\mathbf{b}_{2,des} \times \mathbf{b}_3}{||\mathbf{b}_{2,des} \times \mathbf{b}_3||}, \quad \mathbf{b}_{2,C} = \mathbf{b}_3 \times \mathbf{b}_1, \\ \mathbf{b}_{2,des} &= [-\sin \psi_{des}, \quad \cos \psi_{des}, \quad 0]^\top, \quad \mathbf{b}_{3,C} = \frac{\mathbf{f}}{||\mathbf{f}||}. \end{aligned}$$

For perching on a planar surface, this ψ_{des} can be any angle desired by the user. Generally, we select it such that $\mathbf{b}_{2,des}$ is parallel to \mathbf{s}_2 , which can be know from \mathbf{R}_S . The commanded angular rate is then

$$\hat{\Omega}_C = \mathbf{R}_C^\top \dot{\mathbf{R}}_C. \quad (13)$$

For practical purposes, it is desirable for most of the rotation to be completed before target interception. This is to stop the front of the quadrotor from bouncing off the target and failing to adhere to the target. This aspect is expressed by enforcing an additional acceleration range by a given q tolerance in proximity of the target. In order to apply the inequality constraint to our optimization, we discretize the equation as

$$\begin{aligned} (\alpha\mathbf{s}_3 - g\mathbf{e}_3) &\leq \ddot{\mathbf{x}}(t) \leq (1 + q)(\alpha\mathbf{s}_3 - g\mathbf{e}_3), \\ \forall t \in \{t_f - t_k + j * dt\}, \quad j &\in \mathbb{Z} \ \& \ 0 \leq j < \frac{t_k}{dt}, \end{aligned} \quad (14)$$

where dt is the sampling time of our trajectory planner and t_k is the time prior to the impact which is user defined.

2) *Perching Perception and Physical Constraints:* When perching at a very steep angle such as 90° the endpoint velocity \mathbf{v} can have a large effect on the perching path. This can either aid or greatly hinder the ability to see the target depending on if the quadrotor is ascending or descending to

	$\mathbf{v}_{S3} = 0$	$\mathbf{v}_{S3} = 1$	$\mathbf{v}_{S3} = 2$
$\mathbf{v}_{S1} = \text{Null}$	65.5% / 70.3%	78.1% / 63.9%	85.1% / 65.1%
$\mathbf{v}_{S1} = -3$	68.9% / 72.5%	79.8% / 62.5%	85.6% / 65.8%
$\mathbf{v}_{S1} = -2$	77.5% / 83.7%	85.1% / 75.1%	53.4% / 60.7%
$\mathbf{v}_{S1} = -1$	29.8% / 33.4%	41.3% / 48.3%	43.6% / 45%
$\mathbf{v}_{S1} = 0$	22.4% / 10.4%	33.9% / 27.9%	38.5% / 34.2%
$\mathbf{v}_{S1} = 1$	17.8% / 8.04%	27.0% / 20.4%	25.1% / 29.7%

Table I

PERCENT OF THE TIME / PERCENT OF DISTANCE SUCH THAT THE TRAJECTORY HAS THE TARGET IN ITS FoV AS A FUNCTION OF \mathbf{v}_{S1} AND \mathbf{v}_{S3} . VELOCITIES ARE IN m/s.

intercept. In order to characterize the effects of endpoint velocity on the FoV, we analyze how various endpoints velocities change the path and how well this trajectory maintains the target in the field of view for a trajectory. For our study, we consider two main factors: the percent of time that the trajectory respects the FoV constraint and the ratio between the arc length where the FoV is respected over the full path's length. The qualitative and quantitative results of this study is demonstrated in table (I) and Fig. 7. Here, we consider mainly the following two components $\mathbf{v}_{S1} = \mathbf{v} \cdot \mathbf{S}_1$ and $\mathbf{v}_{S3} = \mathbf{v} \cdot \mathbf{S}_3$, where \mathbf{v}_{S1} is the velocity normal to the landing pad and \mathbf{v}_{S3} is the direction parallel to the landing pad. For the experiments in table (I), we set the same time for each of the trajectories executed in table (I). From Fig. 7, we notice the effect of varying \mathbf{v}_{S1} . As \mathbf{v}_{S1} approaches negative infinity the maximum height is grows higher and for the reverse as \mathbf{v}_{S1} approaches infinity the minimum height of the path dramatically decreases. \mathbf{v}_{S3} does not influence the maximum height or dip of perching, but instead influences where the maximum or minimum dip happens. The faster the normal velocity is the closer to the start the hump will occur. In a generic use case, \mathbf{v}_{S3} will also need to be tuned to meet the perching mechanism. However, for our Velcro mechanism, we experimentally verified that any \mathbf{v}_{S3} is sufficient to achieve perching. The larger this value is the more the vehicle will ascend and descend. We employ the combination of \mathbf{v}_{S1} and \mathbf{v}_{S3} based on our simulation results below to optimize the percent of the trajectory that respects the FoV constraint.

Finally, after the optimization in eq. (5) is solved, we must ensure that the actuator constraint is met

$$\tau_{min}^2 \leq \|m\ddot{\mathbf{x}} + m\mathbf{g}\mathbf{e}_3\|_2^2 \leq \tau_{max}^2 \quad (15)$$

where τ_{min} and τ_{max} are the minimum and maximum thrust respectively. This condition unlike the other previous conditions must be true for the entire trajectory flight time rather than a specific time frame. As a result, it is very difficult to incorporate in the QP optimization described in eq. (5). Direct incorporation to the optimization problem would increase the solving time to be on the order of seconds. Therefore, we perform an efficient bounds check post solving using the Global Bound Checking algorithm 1 from [1, 40]. Details about proof of this algorithm are provided in Section VII. This algorithm returns true if given some polynomial $H(t)$ and some constant b , then $H(t) < b$ for all $t \in [t_0, t_f]$. Otherwise it returns false. Since we use polynomial splines to characterize our trajectory, the thrust is a polynomial. We apply the global bound checker after solving the QP optimization to check if

Algorithm 1 GLOBAL BOUND CHECKING (GBC) [1]

Returns true if $H(t) < b \forall t \in [t_0, t_f]$. $H(t)$ is any polynomial. $b \in \mathbb{R}$ is an upper bound

```

1: Let  $F(t) = H(t) - b$ ;
2: if  $F(t_0) > 0$  or  $F(t_f) > 0$  then
3:   return FALSE
4: end if
5: if STURM( $F(t), t_0, t_f$ ) > 0 then
6:   return FALSE
7: end if
8: return TRUE

```

eq. (15) is respected. Should this constraint not be respected, we iteratively add time to each segment of the polynomial till the constraint is respected. This procedure takes place primarily after solving the initial planning. This is because the combined result of all the newly planned trajectories tends to follow a shorter trajectory and moving at a lower average speed then a one-shot approach as we observe in the experimental section with Fig. 10.

3) *Feasibility Conditions*: Finally, there exists the possibility that the visibility constraint will not be compatible with the perching constraints. In order to verify the existence of this case, we employ the Karush–Kuhn–Tucker (KKT) conditions. The KKT conditions for our quadratic programming defined by eq. (5) with constraints specified in eqs. (8), (12), and (14) determine if a solution exists and what it is. For simplicity, we consider the inequality constraint $\mathbf{y} \leq \mathbf{G}\mathbf{c} \leq \mathbf{z}$ as a simpler inequality constraint $\mathbf{y} \leq \mathbf{G}\mathbf{c}$. It is trivial to rewrite an inequality constraint $\mathbf{G}\mathbf{c} \leq \mathbf{z}$ as an equivalent constraint $-\mathbf{z} \leq -\mathbf{G}\mathbf{c}$ and doing so simplifies our KKT conditions. Solving the KKT conditions involves creating two sets of Lagrange multipliers $\lambda_1 \in \mathbb{R}^J$, $\lambda_2 \in \mathbb{R}^K$, and a group of slack variables $\mathbf{s} \in \mathbb{R}^K$ where J and K are the number of equality and inequality constraints respectively. Based on these new variables, we can formulate the KKT conditions as

$$\begin{aligned}
0 &= \mathbf{Q}\mathbf{c} - \mathbf{A}\lambda_1 - \mathbf{G}\lambda_2, & 0 &= \lambda_1^T (\mathbf{y} - \mathbf{G}\mathbf{c}), \\
0 &= \mathbf{A}\mathbf{c} - \mathbf{b}, & 0 &= \mathbf{G}\mathbf{c} - \mathbf{y} - \mathbf{s}, \\
0 &\leq \lambda_1, \lambda_2, \mathbf{s}.
\end{aligned} \quad (16)$$

We can solve these conditions using the Primal-Dual Interior-Point Method. In the case of divergence, we consider no solution to exist. In case of no solution exists, there is an incompatibility between the FoV constraints and other objectives or constraints in our optimization problem. Therefore, we relax it by removing the FoV constraint and plan the trajectory by only incorporating the perching constraint.

VI. EXPERIMENTAL RESULTS

The experiments are conducted at the Agile Robotics and Perception Lab (ARPL) lab at New York University in a flying arena size $10 \times 6 \times 4 \text{ m}^3$. System navigation is performed solely based on the on-board VIO system running at 300 Hz combined with an Unscented Kalmann Filter [12]. A Vicon²

²www.vicon.com

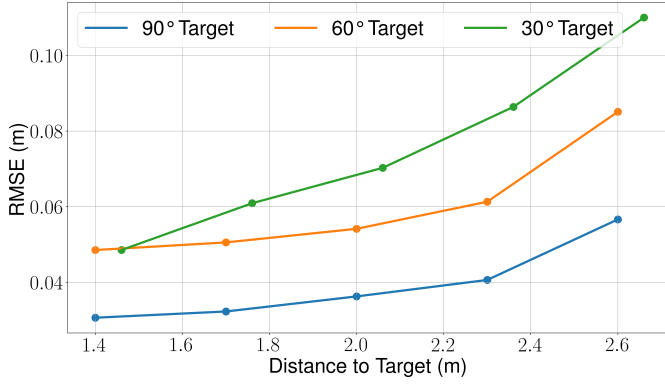


Figure 8. AprilTag localization error as a function of distance from the target at various inclines.

motion capture system is used to record the ground truth data for comparison at 100 Hz. Our landing pad is mounted on an adjustable desk that allows us to control height. In addition, the adhesive is attached to an adjustable stand which allows us to control the surface angle along a specific axis. We selected a tolerance, $q = 0.1$, sampling time, $dt = 0.01$ s, time before impact, $t_k = 0.15$ s and $\alpha = 4.0$ m/s² as the hyperparameters of eqs. (12) and (14). We choose to minimize the $j = 4$, snap norm, for eq. (4). We perform target localization at a rate of 9 Hz, and Active Visual Perching at a rate of 30 Hz for replanning. This planning rate was based on the average execution time of each individual planning being 27 mS to complete on-board. In our perching constraints, we set $v_{S1} = -2$ and $v_{S1} = 0.3$. The slight increase of $v_{S1} = 0.3$ from the optimal $v_{S1} = 0$ is because Velcro needs some forward momentum to attach itself. As a heuristic, we found that 0.3 was a good amount of forward momentum to attach to the landing pad. In this section, we demonstrate the improvement in target localization gained from using multiple detection on approach. Next, we will show that perform active visual planning greatly reduces the RMSE between desired and planned action in both simulation in the real world. Finally, we demonstrate that we can successfully perch on any target up to 90° using this method with only on-board sensing.

A. Target Localization

For all vision based localization methods as the distance between camera and target reduces, the target localization improves. In this experiment, we demonstrate this concept by flying a quadrotor level to the target and backing away horizontally to measure the localization error from the Apriltag and compare it to the ground truth pose values obtained using our Vicon motion capture system. This procedure is repeated at multiple inclines where the angle refers to the relative angle between the floor and target. The results are recorded in Fig. 8. As seen in Fig. 8, a further distance causes the target localization error to exponentially increase. This clearly motivates the need for replanning in our system, we will also later see that closing this error translates into a real visible improvement in perching consistency.

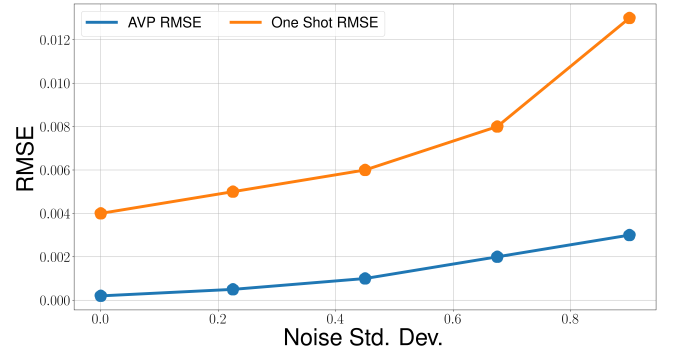


Figure 9. The control error as a function of the error's standard deviation in the simulator. In the simulator, the quadrotor was tasked with perching on a target 1.7 m away at an incline of 90°.

B. Active Visual Planning Simulation

In this experiment, we aim to study how injecting greater error in eq. (2) for the terms e_R, e_Ω, e_x, e_v would scale with the tracking error. This experiment is performed in simulation where the noise is controllable. Zero mean Gaussian noise with different variance ranging from 0 – 1 is injected into the error terms of eq. (2). After injecting the noise into the error terms, we set the quadrotor to perform a standard perching trajectory on a 90° incline in simulation from a distance of 1.7 m. This experiment was repeated for both a one-shot and AVP approach. The tracking RMSE between the planned and true path is reported in Fig. 9. The proposed AVP approach shows increased robustness to injected noise in the localization compared to the one-shot planning case.

C. Analysis of Target Localization Effects

In this scenario, in order to characterize the effect of AVP without the potential drift effect of our on-board VIO, we use the Vicon system for quadrotor localization and still employ the camera for the target detection and localization. In our first experiment, we use the Vicon system as feedback for our odometry and the front camera to localize the targets' location. For one set of flights, we perform only one planning based on the initial target localization, and the second, we perform the AVP method mentioned in Section (V). The vehicle initially flies to a hovering position to the same height as the target and detects it. To simplify plotting, we align the y axis of the vehicle and the target. This is not required for perching as we demonstrate in our attached multimedia material, but it is helpful for visualization and explanation purposes. The vehicle performs on-board computations and tries to intercept the target once a command has been given by an external base station to start the maneuver. No major computations occur on the base station. The base station is simply there to give commands. The entire control, planning, and target localization pipeline takes place on-board the vehicle. Vehicle estimation exclusively is left to the Vicon in this this section. This experiment was repeated five times at varying inclinations of the target and distances. The results were recorded on table (II). Results in Table (II) show a reduced tracking error when landing the target compared to performing a one-shot.

	Axis	1.7 m		3 m	
		One Shot	AVP	One Shot	AVP
60°	x (m)	0.016	0.026	0.021	0.06
	y (m)	0.01	0.001	0.007	0.001
	z (m)	0.122	0.012	0.064	0.009
90°	x (m)	0.015	0.015	0.014	0.09
	y (m)	0.01	0.001	0.016	0.003
	z (m)	0.111	0.013	0.064	0.019

Table II
TRACKING RMSE COMPARISON BETWEEN AVP AND ONE-SHOT PLANNING.

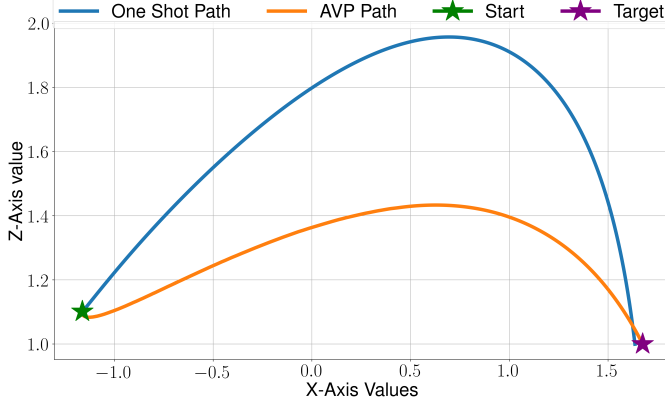


Figure 10. Path Comparison between the one-shot and the AVP on the X and Z axis. Y-axis is left out to improve visualization and set to constant zero. This experiment was done trying to land on a 90° inclined surface with the $v_{s1} = -2$ and $v_{s3} = 0.3$. Slight deviations between the end and start points are due to slight difference in AprilTag detection for real world experiments and drift when take off. One-shot perching is done with the Vicon for its path estimation.

D. Active Visual Perching Experiments

Finally, we demonstrate the ability of our quadrotor to perform aggressive maneuvers solely using VIO without any external sensors. These experiments have the same set-up as in Section VI-C with the exception that in this case vehicle localization is now performed on-board using the bottom camera with the VIO. The Vicon motion capture system collects ground truth data to calculate the estimation loss. This experiment was repeated ten times in a row and we recorded the success/failure rates of our trials. Another interesting property that comes out of these executed trajectory between one-shot and AVP is that the executed trajectories can be quite different even with highly accurate state estimation. This is demonstrated in Fig. 10 for a path with a 90° perching maneuver for a one-shot perching AVP cases. We notice that the executed path for the one-shot trajectory case is quite different compared to the AVP trajectory. On the other hand, the difference between AVP with Vicon for is not substantially different compared to with VIO for state estimation. The difference in paths between Vicon and VIO is likely due to VIO tracking error and variance in Apriltag localization between the two trajectories. Overall, in our tests we noticed that our AVP planner preferred a shorter in terms of distance. During our tests, our quadrotor reached a maximum angular speed of 750 deg/s showing that despite the high angular velocity demonstrated in Fig. 12 perching is still achievable with only on-board computation. We also include a visualization of the successful perching trajectory performed in Fig. 11 for a three

	Axis	1.7 m		3 m	
		Tracking	Estimation	Tracking	Estimation
60°	x (m)	0.05	0.09	0.053	0.013
	y (m)	0.004	0.068	0.001	0.078
	z (m)	0.02	0.094	0.018	0.03
90°	x (m)	0.121	0.115	0.09	0.222
	y (m)	0.005	0.005	0.02	0.019
	z (m)	0.067	0.05	0.03	0.055

Table III
TRACKING AND CONTROL RMSE FOR PERCHING USING VISUAL INERTIAL ODOMETRY AND AVP .

meter flight. Overall, we see that initially the estimation and tracking is loss is low till it diverges at the end due to higher angular rates incurred by perching on a vertical object. We quantify these results in Table III, where we notice that as expected less aggressive maneuvers like perching on 60° has less tracking error than a more aggressive maneuver. Finally compared to our previous work [1], we performed 10 trials and saw that our success rate has improved by doing AVP over a one-shot approach by 10% for both the 1.7 m and the 3 m cases.

VII. CONCLUSION

In this paper, we proposed an AVP strategy that exploits new mid-flight information such as the vehicle odometry and new target localization to improve the robustness to localization and control errors of our perching task compared to a one-shot approach. We theoretically and experimentally showed how to efficiently formulate and execute this problem as a QP optimization that incorporates actuator and FoV constraints. The KKT conditions further guarantee the feasibility of the planned maneuver. We experimentally analyze the effects of different boundary conditions on the spatio-temporal target visibility during the perching maneuver and identify the best choice able to maximize it. The proposed AVP consistently shows superior performances compared to a one-shot planning approach. This algorithm is still light weight to run on-board concurrently with the target localization, on-board VIO, and control during flight.

Future works will focus on intercepting a moving target fully exploiting the potential of our planner to adapt in mid flight. Additionally, it is relevant to improve our controller to incorporate other high speed dynamic effects or disturbances such as drag. We would also like to exploit past perching iterations to further refined the maneuver in a learning-based fashion. Finally, we would also like to explore the possibility to consider a more general object or surface detection algorithm to remove the need for fiducial marker. This would also facilitate the execution of perching experiments in outdoor settings.

REFERENCES

- [1] J. Mao, G. Li, S. M. Nogar, C. M. Kroninger, and G. Loianno, "Aggressive visual perching with quadrotors on inclined surfaces," 2021 *IEEE/RSJ International Conference on Intelligent Robots and Systems (IROS)*, 2021.
- [2] C. Richter, A. Bry, and N. Roy, "Polynomial trajectory planning for aggressive quadrotor flight in dense indoor environments," *Robotics research*, pp. 649–666, 2016.

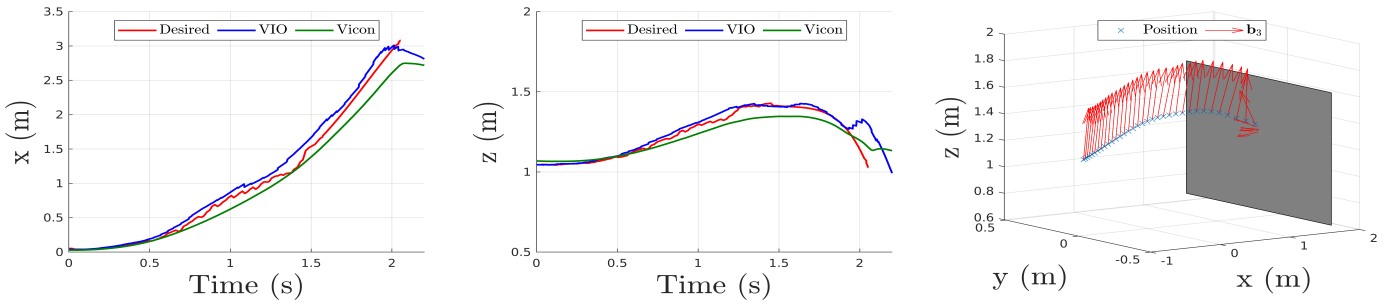


Figure 11. Trajectory tracking and localization visualization for perching on a 90° surface inclination from a distance of 3 m. The blue crosses represent the quadrotor position, whereas the arrows represent the thrust vector. The Y-axis has been left out because the target and vehicle are aligned on the axis. This is not a requirement as demonstrated in the multimedia attachment but improves visualization.

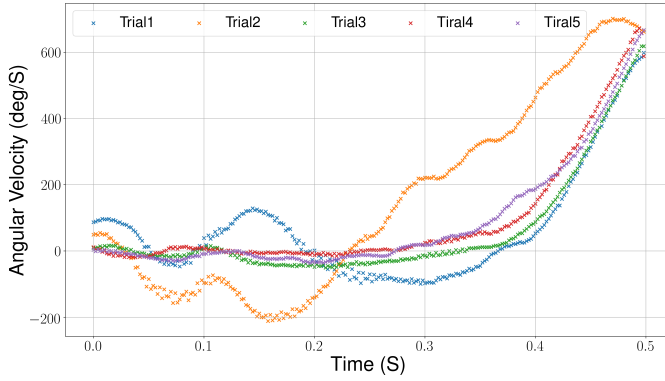


Figure 12. Angular rate of the b_2 during a 90° perching maneuver 5 Trial demonstrations. Other axes b_1 and b_3 were left out because the angular rates on them were minimum.

- [3] Z. Wang, X. Zhou, C. Xu, and F. Gao, "Alternating minimization based trajectory generation for quadrotor aggressive flight," *IEEE Robotics and Automation Letters (RAL)*, vol. 5, pp. 4836–4843, 2020.
- [4] F. Gao, W. Wu, J. Pan, B. Zhou, and S. Shen, "Optimal time allocation for quadrotor trajectory generation," *2018 IEEE/RSJ International Conference on Intelligent Robots and Systems (IROS)*, pp. 4715–4722, 2018.
- [5] D. Burke, A. Chapman, and I. Shames, "Generating minimum-snap quadrotor trajectories really fast," *2020 IEEE/RSJ International Conference on Intelligent Robots and Systems (IROS)*, pp. 1487–1492, 2020.
- [6] M. Watterson, S. Liu, K. Sun, T. Smith, and V. Kumar, "Trajectory optimization on manifolds with applications to quadrotor systems," *The International Journal of Robotics Research (IJRR)*, vol. 39, no. 2-3, pp. 303–320, 2020.
- [7] S. Liu, K. Mohta, N. Atanasov, and V. Kumar, "Search-based motion planning for aggressive flight in $se(3)$," *IEEE Robotics and Automation Letters (RAL)*, vol. PP, 10 2017.
- [8] V. Agrawal and F. Dellaert, "Continuous-time state and dynamics estimation using a pseudo-spectral parameterization," *2021 IEEE International Conference on Robotics and Automation (ICRA)*, pp. 426–432, 2021.
- [9] P. Foehn and D. Scaramuzza, "CPC: complementary progress constraints for time-optimal quadrotor trajectories," *Preprint*, 2020.
- [10] F. Morbidi, R. Cano, and D. Lara, "Minimum-energy path generation for a quadrotor uav," *2016 IEEE International Conference on Robotics and Automation (ICRA)*, pp. 1492–1498, 2016.
- [11] J. Thomas, M. Pope, G. Loianno, E. Hawkes, M. Estrada, H. Jiang, M. Cutkosky, and V. Kumar, "Aggressive flight for perching on inclined surfaces," *Journal of Mechanisms and Robotics*, vol. 8, 12 2015.
- [12] G. Loianno, C. Brunner, G. McGrath, and V. Kumar, "Estimation, control, and planning for aggressive flight with a small quadrotor with a single camera and imu," *IEEE Robotics and Automation Letters (RAL)*, vol. PP, pp. 1–11, 11 2016.
- [13] Y. Chen and N. O. Pérez-Arancibia, "Controller synthesis and performance optimization for aerobatic quadrotor flight," *IEEE Transactions on Control Systems Technology (TCST)*, vol. 28, no. 6, pp. 2204–2219, 2020.

- [14] S. Lupashin, A. Schöllig, M. Sherback, and R. D'Andrea, "A simple learning strategy for high-speed quadcopter multi-flips," *2010 IEEE International Conference on Robotics and Automation (ICRA)*, pp. 1642–1648, 2010.
- [15] E. Kaufmann, A. Loquercio, R. Ranftl, M. Müller, V. Koltun, and D. Scaramuzza, "Deep drone acrobatics," *Robotics: Science and Systems (RSS)*, 2020.
- [16] J. Thomas, G. Loianno, K. Daniilidis, and V. Kumar, "Visual servoing of quadrotors for perching by hanging from cylindrical objects," *IEEE Robotics and Automation Letters (RAL)*, vol. 1, no. 1, pp. 57–64, 2016.
- [17] H. Zhang, B. Cheng, and J. Zhao, "Optimal trajectory generation for time-to-contact based aerial robotic perching," *Bioinspiration & Biomimetics*, vol. 14, 10 2018.
- [18] W. Chi, K. H. Low, K. H. Hoon, and J. Tang, "An optimized perching mechanism for autonomous perching with a quadrotor," *IEEE International Conference on Robotics and Automation (ICRA)*, pp. 3109–3115, 2014.
- [19] K. M. Popek, M. S. Johannes, K. C. Wolfe, R. A. Hegeman, J. M. Hatch, J. L. Moore, K. D. Katyal, B. Y. Yeh, and R. J. Bamberger, "Autonomous grasping robotic aerial system for perching (agrasp)," *2018 IEEE/RSJ International Conference on Intelligent Robots and Systems (IROS)*, pp. 1–9, 2018.
- [20] W. Roderick, M. Cutkosky, and D. Lentink, "Bird-inspired dynamic grasping and perching in arboreal environments," *Science Robotics*, vol. 6, no. 61, p. eabj7562, 2021.
- [21] A. Kalantari, K. Mahajan, D. Ruffatto, and M. Spenko, "Autonomous perching and take-off on vertical walls for a quadrotor micro air vehicle," *IEEE International Conference on Robotics and Automation (ICRA)*, pp. 4669–4674, 2015.
- [22] E. W. Hawkes, D. L. Christensen, E. V. Eason, M. A. Estrada, M. Heverly, E. Hilgemann, H. Jiang, M. T. Pope, A. Parness, and M. R. Cutkosky, "Dynamic surface grasping with directional adhesion," *IEEE/RSJ International Conference on Intelligent Robots and Systems (IROS)*, pp. 5487–5493, 2013.
- [23] L. Daler, A. Klaptocz, A. Briod, M. Sitti, and D. Floreano, "A perching mechanism for flying robots using a fibre-based adhesive," *2013 IEEE International Conference on Robotics and Automation (ICRA)*, pp. 4433–4438, 2013.
- [24] C. C. Kessens, J. Thomas, J. P. Desai, and V. Kumar, "Versatile aerial grasping using self-sealing suction," *IEEE International Conference on Robotics and Automation (ICRA)*, pp. 3249–3254, 2016.
- [25] S. Backus, J. Izraelevitz, J. Quan, R. Jitosh, E. Slavick, and A. Kalantari, "Design and testing of an ultra-light weight perching system for sloped or vertical rough surfaces on mars," *2020 IEEE Aerospace Conference*, pp. 1–12, 2020.
- [26] H. W. Wopereis, T. D. van der Molen, T. H. Post, S. Stramigioli, and M. Fumagalli, "Mechanism for perching on smooth surfaces using aerial impacts," *2016 IEEE International Symposium on Safety, Security, and Rescue Robotics (SSRR)*, pp. 154–159, 2016.
- [27] S. Park, D. S. Drew, S. Follmer, and J. Rivas-Davila, "Lightweight high voltage generator for untethered electroadhesive perching of micro air vehicles," *IEEE Robotics and Automation Letters (RAL)*, vol. 5, no. 3, pp. 4485–4492, 2020.
- [28] M. T. Pope, C. W. Kimes, H. Jiang, E. W. Hawkes, M. A. Estrada, C. F. Kerst, W. R. T. Roderick, A. K. Han, D. L. Christensen, and M. R. Cutkosky, "A multimodal robot for perching and climbing on vertical

- outdoor surfaces,” *IEEE Transactions on Robotics (T-RO)*, vol. 33, no. 1, pp. 38–48, 2017.
- [29] J. Moore, R. Cory, and R. Tedrake, “Robust post-stall perching with a simple fixed-wing glider using lqr-trees,” *Bioinspiration & Biomimetics*, vol. 9, p. 025013, 05 2014.
- [30] A. L. Desbiens, A. T. Asbeck, and M. R. Cutkosky, “Landing, perching and taking off from vertical surfaces,” *The International Journal of Robotics Research (IJRR)*, vol. 30, no. 3, pp. 355–370, 2011.
- [31] D. Mehanovic, J. Bass, T. Courteau, D. Rancourt, and A. L. Desbiens, “Autonomous thrust-assisted perching of a fixed-wing uav on vertical surfaces,” *Conference on Biomimetic and Biohybrid Systems*, pp. 302–314, 2017.
- [32] E. Olson, “AprilTag: A robust and flexible visual fiducial system,” *2011 IEEE International Conference on Robotics and Automation (ICRA)*, pp. 3400–3407, May 2011.
- [33] V. Usenko, L. Von Stumberg, A. Pangercic, and D. Cremers, “Real-time trajectory replanning for mavs using uniform b-splines and a 3d circular buffer,” *2017 IEEE/RSJ International Conference on Intelligent Robots and Systems (IROS)*, pp. 215–222, 2017.
- [34] B. Zhou, J. Pan, F. Gao, and S. Shen, “Raptor: Robust and perception-aware trajectory replanning for quadrotor fast flight,” *IEEE Transactions on Robotics (T-RO)*, 2021.
- [35] D. Falanga, A. Zanchettin, A. Simovic, J. Delmerico, and D. Scaramuzza, “Vision-based autonomous quadrotor landing on a moving platform,” *2017 IEEE International Symposium on Safety, Security and Rescue Robotics (SSRR)*, pp. 200–207, 2017.
- [36] G. Loianno, C. Brunner, G. McGrath, and V. Kumar, “Estimation, control, and planning for aggressive flight with a small quadrotor with a single camera and imu,” *IEEE Robotics and Automation Letters (RAL)*, vol. 2, no. 2, pp. 404–411, April 2017.
- [37] T. Lee, M. Leok, and N. H. McClamroch, “Nonlinear Robust Tracking Control of a Quadrotor UAV on SE(3),” *Asian Journal of Control*, vol. 15, no. 2, pp. 391–408, 2013.
- [38] G. Loianno, Y. Mulgaonkar, C. Brunner, D. Ahuja, A. Ramanandan, M. Chari, S. Diaz, and V. Kumar, “Smartphones power flying robots,” *2015 IEEE/RSJ International Conference on Intelligent Robots and Systems (IROS)*, pp. 1256–1263, Sept 2015.
- [39] G. Li, A. Tunchez, and G. Loianno, “Pcmpe: Perception-constrained model predictive control for quadrotors with suspended loads using a single camera and imu,” *2021 IEEE International Conference on Robotics and Automation (ICRA)*, 2021.
- [40] C. Sturm, “Collected works of charles franois sturm,” *Inst. France Sc. Math. Phys.*, vol. 6, pp. 345–390, 01 2009.

APPENDIX

A. Sturm’s Theorem

Sturm’s theorem [40] states that the number of roots for a polynomial, $H(t)$ in an interval $[t_0, t_f]$ is equal to the difference in sign changes of the Sturm’s sequence, eq. (17), between $S(t_0)$ and $S(t_f)$

$$S(t) = \begin{cases} S_0(t) = H(t) \\ S_1(t) = \dot{H}(t) \\ S_{i+1}(t) = -Rm(S_{i-1}, S_i) \\ \vdots \\ S_N(t) = -Rm(S_{N-2}, S_{N-1}) \in \mathbb{R} \end{cases}, \quad (17)$$

where $Rm(S_{i-1}, S_i)$ gives the algebraic remainder of $\frac{S_{i-1}}{S_i}$. To evaluate the number of roots between $t \in [0, 2]$ for $H(t) =$

$t^4 + t^3 - t - 1$. First calculate the Sturm sequence,

$$S(t) = \begin{cases} S_0(t) = t^4 + t^3 - t - 1 \\ S_1(t) = 4t^3 + 3t^2 - 1 \\ S_2(t) = 0.1875t^2 + 0.75t + 0.9375 \\ S_3(t) = -32t - 64 \\ S_4(t) = -0.1875 \end{cases}. \quad (18)$$

We evaluate this sequence’s signs at $t = 0$ as $[-, -, +, -, -]$. This sequence has 2 sign changes. Next, we calculate the sequence at $t = 2$ as $[+, +, +, -, -]$. There is 1 sign change. Subtracting the number of sign changes at $t = 0$ from $t = 1$, we find 1 root for $H(t)$ in the domain $[0, 2]$.

B. Proof of Algorithm 1

First, we leverage the intermediate value theorem. The intermediate value theorem state that given a continuous function $H(t)$ whose domain contains the values $[t_0, t_f]$ then $\forall i \in [H(t_0), H(t_f)]$ there must exist a corresponding $t_i \in [t_0, t_f]$ such that $i = H(t_i)$. Since our trajectory is continuous, this theorem holds in our case. Now let’s prove that our algorithm works by contradiction. Assume, there exists a $t_i \in [t_0, t_1]$ such that $H(t_i) > b$ where b is the global bound, and all conditions of Algorithm 1, $H(t_0) < b$, $H(t_f) < b$, and $H(t_i) - b \neq 0 \forall t_i \in [t_0, t_f]$ are true.

If this is the case, then we can apply the intermediate value theorem and construct a domain $[t_0, t_i]$ and a range $[H(t_0), H(t_i)]$. We know that $H(t_0) < b$ and $H(t_i) > b$, then $b \in [H(t_0), H(t_i)]$. Therefore, based on the intermediate value theorem, there must exist a $t_j \in [t_0, t_i]$ such that $H(t_j) = b$. However, we see $H(t_j) = b$ is a contradiction with respect to the condition $H(t_j) - b \neq 0 \forall t_j \in [t_0, t_f]$. As $[t_0, t_i] \subset [t_0, t_f]$ by construction, this condition also holds true for all $t_j \in [t_0, t_i]$. Since, this is a contradiction there can exist no such number $t_i \in [t_0, t_1]$ such that $H(t_i) > b$ if our algorithm returns true.